Influence of ion implantation parameters on the perpendicular magnetic anisotropy of Fe-N thin films with stripe domains

T. Amarouche, Lucas Garnier, M. Marangolo, M. Eddrief, Victor H. Etgens, F. Fortuna, Y. Sadaoui, M. Tamine, J. L. Cantin, H. J. von Bardeleben

Influence of ion implantation parameters on the perpendicular magnetic anisotropy of Fe-N thin films with stripe domains

T. Amarouche,[1,2,a)] L.-C. Garnier,[2,3] M. Marangolo,[2] M. Eddrief,[2] V. H. Etgens,[2,3,4] F. Fortuna,[5,6] Y. Sadaoui,[1] M. Tamine,[1] J. L. Cantin,[2] and H. J. von Bardeleben[2]

[1]*Laboratoire de Physique et Chimie Quantique, Univ. Mouloud Mammeri, 15000 Tizi-Ouzou, Algeria*

[2]*Sorbonne Universités, UPMC Univ. Paris 6, CNRS, Institut des NanoSciences de Paris, 4 place Jussieu, 75005 Paris, France*

[3]*Université Versailles St-Quentin, LISV, Bâtiment Boucher, Pôle Scientifique et Technique de Vélizy, 10–12 Avenue de l'Europe, 78140 Vélizy, France*

[4]*Univ. Paris-Sud, CSNSM, UMR 8609, Bâtiments 104 et 108, 91405 Orsay, France*

[5]*CNRS IN2P3, 91405 Orsay, France*

[6]*Institut VEDECOM, 77 rue des Chantiers, 78000 Versailles, France*

Nitrogen-martensite thin films are known to present a perpendicular magnetic anisotropy (PMA) depending on the nitrogen content. Additionally, weak magnetic stripe domains have been studied in Fe-N samples made by ion implantation. In this work, ion implantation proves to be a good technique to make nitrogen-martensite thin films presenting both tunable PMA and stripe domains. We report on the changes in magnetic and structural properties of nitrogen-implanted iron thin films, resulting from various implantation conditions. Fluences from 1.8×10^{16} N_2^+/cm^2 to 3.5×10^{16} N_2^+/cm^2 at 26 keV and 5.3×10^{16} N_2^+/cm^2 at 40 keV were used to implant iron thin films epitaxially grown on ZnSe/GaAs(001). X-ray diffraction measurements disclosed the presence of body-centered tetragonal nitrogen-martensite whose c-axis is perpendicular to the thin film plane and the c-parameter increases with fluence. Vibrating sample magnetometer measurements revealed that nitrogen implantation induced strong changes in magnetic properties such as an increasing PMA with fluence. Therefore, this PMA may originate from the magnetocrystalline anisotropy of nitrogen-martensite and stress-induced anisotropy. Magnetic stripe domains are notably observed by magnetic force microscopy for the highest fluences. Furthermore, ferromagnetic resonance measurements lead to the magnetic anisotropy constants calculation. The results show a significant increase of the PMA, related to the presence of nitrogen-martensite whose c-parameter is close to that of α'-Fe_8N, which reaches a maxi-mum value of 4.9×10^6 erg/cm^3. In addition, an interesting comparison is done between the anisot-ropy constants of Fe-N and Fe-Ga samples. Fe-Ga thin films are also well known to present PMA and stripe domains.

I. INTRODUCTION

Ferromagnetic thin films with perpendicular magnetic anisotropy (PMA) are of great interest for the development of new technologies in the field of modern magnetism. PMA is a remarkable behavior that tends to align the thin film magnetization along the direction perpendicular to the film plane, whereas the thin film shape strongly favors magnetization parallel to the film plane. Many studies have been done on PMA materials that can be used in spintronics devices.[1–5] Additionally, thin films with PMA present different magnetic domain patterns as weak stripe domains,[6] which might be useful for magnonics applications thanks to specific resonance modes.[7] Interestingly, binary iron-based systems such as Fe-N and Fe-Ga can lead to thin films having PMA depending on the concentration of nitrogen and gallium, respectively, and chemical ordering.[8,9] Moreover, both materials present weak stripe domains at remanence.[10,11] More precisely, nitrogen-martensite presents a magnetocrystalline anisotropy (MCA) due to its body-centered tetragonal (bct) structure and is known to develop PMA in thin films.[12] Usually defined as α', this Fe-N phase can contain a varying amount of nitrogen.[13] The nitrogen atoms are randomly located in one third of the octahedral voids inside the bct iron lattice. The c/a ratio of lattice parameters increases with increasing nitrogen amount and is maximum for α'-Fe_8N. It is possible to tune the PMA in nitrogen-martensite thin films by controlling the nitrogen concentration in the material.[8] The PMA is strong when α'-Fe_8N is formed, and increases with nitrogen ordering.[8,14] The chemically ordered iron nitride α''-$Fe_{16}N_2$ is well known for its possible giant saturation magnetization[15] and large MCA.[14] Fe-N thin films with PMA also play an important role in the study of weak magnetic stripe domains. Garnier *et al.* recently reported on the behavior of those stripe domains in nitrogen-martensite thin films made by ion implantation.[10] Concerning Fe-Ga, Barturen *et al.* highlighted in Fe-Ga thin films epitaxially grown on ZnSe/GaAs(001), a PMA depending on gallium concentration.[9] A maximum perpendicular energy density of about 5×10^6 erg/cm^3 has been reported for a sample with 20% at. Ga. This PMA has been attributed to the ordering of Ga pairs aligned along the [001] growth direction. Ga pairing

[a)]Author to whom correspondence should be addressed: amarouche@insp.jussieu.fr

consequently favors the tetragonal distortion of the Fe-Ga cubic crystalline structure.[16] Weak magnetic stripe domains have also been studied in Fe-Ga thin films.[11] In this study, we show that nitrogen implantation in iron thin films epitaxially grown on ZnSe/GaAs(001) induces varying degrees of PMA depending on implantation parameters such as fluence. This PMA is related to the out-of-plane lattice constant of the bct α'-Fe-N phase formed by ion implantation. Here, α'-Fe-N refers to nitrogen-martensite whose nitrogen concentration differs from that of α'-Fe_8N. We highlight the presence of weak magnetic stripe domains for different sets of implantation parameters. The magnetic anisotropy constants in our Fe-N thin films were deduced from ferromagnetic resonance (FMR) experiments and compared with those of Fe-Ga samples.

II. MATERIAL AND METHODS

A 78-nm-thick body centered cubic (bcc) α-Fe thin film was epitaxially grown on the ZnSe-buffered GaAs(001) substrate in a molecular beam epitaxy (MBE) chamber. Then, the iron film was *in situ* protected against oxidization by the deposition of a gold capping layer with a thickness of 8 nm. Pieces of this single sample were implanted with N_2^+ ions at an energy of 26 keV with fluences from 1.8×10^{16} to 3.5×10^{16} N_2^+/cm^2 and at an energy of 40 keV with a fluence of 5.3×10^{16} N_2^+/cm^2, at room temperature. Details about the sample preparation process are given elsewhere.[10] The concentration depth distribution of nitrogen in the implanted films was measured by Rutherford backscattering spectrometry (RBS) and elastic recoil detection analysis (ERDA) using a 43 MeV Cl^{7+} ion beam. The angle between the sample normal and the incoming beam is 75°, and the scattering angle is 31°. The analyzed area is about 1.5 $\times$ 1.5 mm^2. The recoil ions and the scattered Cl ions have been detected with a Bragg ionization chamber using a full energy detection circuit for the ion energies and a fast timing circuit to obtain a Z dependent signal to separate ion species. All ERDA spectra are fitted simultaneously using the program NDF v9.3gi and the depth profiles are obtained from this fit.[17] The crystalline structure of the as-grown and as-implanted samples was investigated by X-ray diffraction (XRD) measurements using monochromatized Cu Kα radiation. A vibrating sample magnetometer (VSM) was used to perform magnetization measurements at room temperature. To determine the magnetic anisotropy constants of the thin films, ferromagnetic resonance (FMR) measurements were carried out in-plane and out-of-plane, at Q-band and X-band microwave frequencies, respectively, at room temperature in a standard cavity set-up. The FMR results were analyzed with the standard Smit-Beljers formalism.

III. RESULTS AND DISCUSSION

A. Nitrogen distribution

In Fig. 1, we show the depth distribution profiles of nitrogen concentration measured by the combination of ERDA and RBS for samples implanted with 2.2×10^{16} N_2^+/cm^2 at 26 keV and 5.3×10^{16} N_2^+/cm^2 at 40 keV. The nitrogen

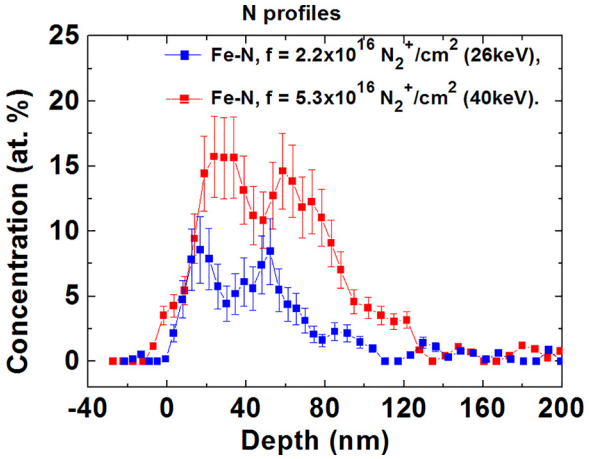

FIG. 1. Nitrogen distribution in the bct α'-Fe-N films obtained from ERDA and RBS measurements, error bars are shown in the figure.

concentration profiles are directly based on the measured spectra. They are convoluted with the system resolution and physical effects like straggling. The nitrogen concentration is obtained from the integrated depth profiles. A quite large statistical uncertainty of the order of 10%, only based on the number of detected nitrogen recoils, is found. Indeed, the count rate is dominated by Cl scattering on Ga and As, which have a much higher cross-section than N. As expected, the mean concentration and penetration depth of nitrogen are higher for 5.3×10^{16} N_2^+/cm^2 at 40 keV than those for 2.2×10^{16} N_2^+/cm^2 at 26 keV. However, the experimental depth distribution profiles are more widespread than those simulated using the transport of ions in matter (TRIM) simulation program.[18] Moreover, both experimental profiles have a similar shape with local maxima. Nevertheless, this observation is not commented here in view of the large error bars (Table I).

B. Crystallographic structure

Figure 2 contains out-of-plane XRD results for the as-grown and nitrogen-implanted samples at 26 keV and 40 keV. For the pristine sample grown by MBE, we observe the α-Fe (002) diffraction peak whose sharpness reflects the high crystalline quality of the epitaxial iron thin film. The gold capping layer is revealed by the Au (002) peak presenting Laüe oscillations. The GaAs (002) and GaAs (004) reflections of the substrate are identified. After nitrogen implantation, the α-Fe (002) line disappeared. For 1.8×10^{16} N_2^+/cm^2 at 26 keV, low-intensity diffracted X-rays are detected for a range of 2θ angles near the α-Fe (002) position. This suggests that the nitrogen-implanted iron thin films contain a poorly crystallized compound whose lattice planes

TABLE I. Nominal and measured (RBS/ERDA) total N doses for the two samples with high fluences.

Sample	Expected dose	Measured dose	Stat. uncertainty
Fe-N 26 keV	2.2×10^{16} N_2^+/cm^2	1.75×10^{16} N_2^+/cm^2	12%
Fe-N 40 keV	5.3×10^{16} N_2^+/cm^2	4.15×10^{16} N_2^+/cm^2	8%

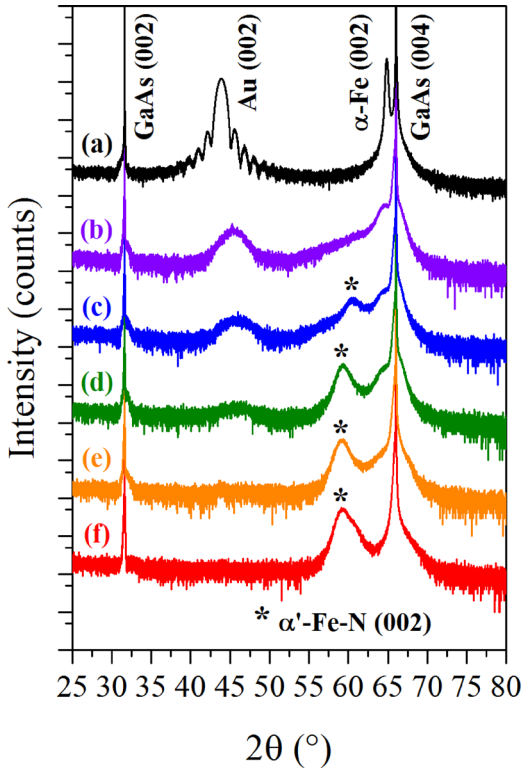

FIG. 2. θ-2θ X-ray scans for the 26 keV and 40 keV implanted Fe-N films as a function of increasing N fluence. (a) As-grown, (b) Fe-N, f = 1.8×10^{16} N_2^+/cm^2 (26 keV), (c) Fe-N, f = 2.2×10^{16} N_2^+/cm^2 (26 keV), d) Fe-N, f = 3.0×10^{16} N_2^+/cm^2 (26 keV), (e) Fe-N, f = 3.5×10^{16} N_2^+/cm^2 (26 keV), and (f) Fe-N, f = 5.3×10^{16} N_2^+/cm^2 (40 keV).

are separated by a distance close to the interplanar spacing between α-Fe (002) planes. From 2.2×10^{16} to 3.5×10^{16} N_2^+/cm^2 at 26 keV, a broad peak whose scattering angle decreases when the fluence increases is assigned as the α′-Fe-N (002) reflection. Hence, nitrogen implantation formed bct α′-Fe-N whose c-axis is perpendicular to the thin film plane and c-parameter increases with fluence following the Bragg's law. In addition, the low-intensity diffracted X-rays detection is still clearly visible near the α-Fe (002) position, except for 3.5×10^{16} N_2^+/cm^2. For 5.3×10^{16} N_2^+/cm^2 at 40 keV, only the broad α′-Fe-N (002) reflection is observed. It is worth noting that the highest fluences at both energies led to the formation of α′-Fe-N whose c-parameter is slightly lower than that of α′-Fe_8N, i.e., 3.14 Å.[13] Among all the implanted samples, the width of the α′-Fe-N (002) peak reflects the low crystalline quality of this phase. Concerning the Au (002) peak, we notice its broadening and its shift towards larger scattering angles with increasing fluence from 1.8×10^{16} N_2^+/cm^2 to 3.0×10^{16} N_2^+/cm^2 at 26 keV. For higher fluences, 3.5×10^{16} N_2^+/cm^2 at 26 keV and 5.3×10^{16} N_2^+/cm^2 at 40 keV, the Au (002) peak is no longer observable. These observations are related to the surface recession of the protecting gold capping layer due to the sputtering effect induced by ion implantation.

C. Magnetization

Figure 3 compares the magnetization curves for nitrogen-implanted iron thin films, taken along in-plane crystallographic directions [100], [110], and out-of-plane crystallographic direction [001]. These VSM measurements were done for samples implanted with different ion energies and fluences. Besides, the magnetization curves of the pristine iron thin film are shown in the insets to provide a reference. Concerning in-plane measurements, the hysteresis loops have differences in shape as a function of the implantation parameters. The implanted sample with 1.8×10^{16} N_2^+/cm^2 at 26 keV exhibits a similar behavior to that of the pristine iron

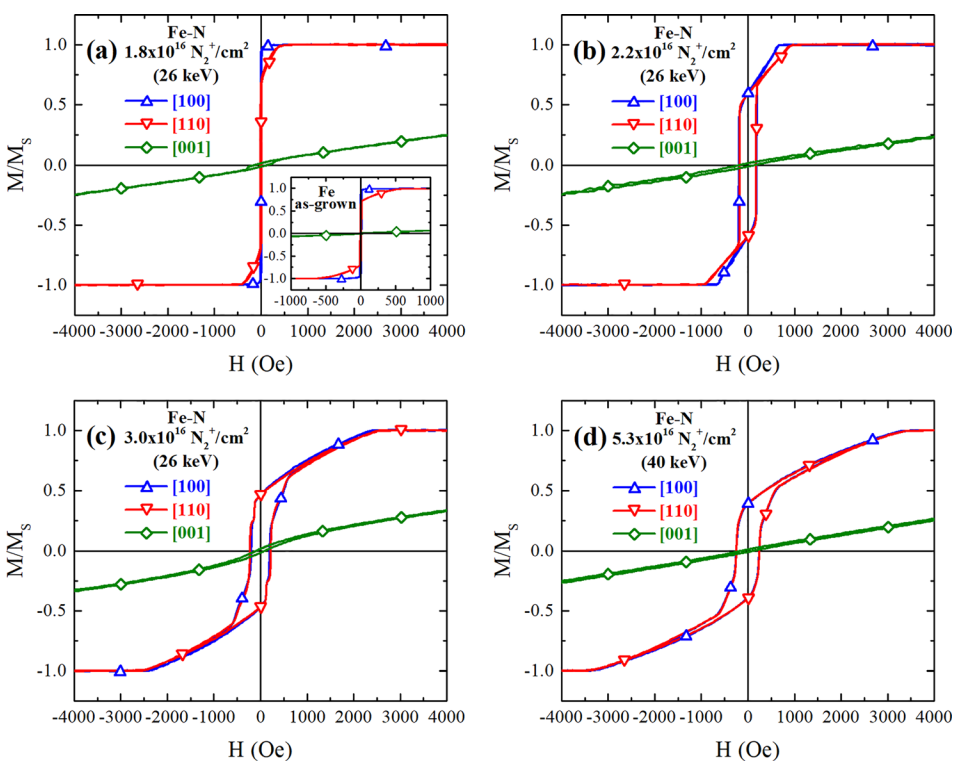

FIG. 3. VSM measurements of Fe-N thin films epitaxied on ZnSe/GaAs (001) (in the insert, the axes are the same as for the parent figure.).

sample. The axis along [100] is easier than the axis along [110]. For 2.2×10^{16} N_2^+/cm^2 at 26 keV, the coercivity and the saturation field increase and the reduced magnetization at remanence decreases compared with the sample previously described. In addition, the in-plane magnetization curves display a small region where the magnetization changes linearly with the applied magnetic field. The axis along [100] is still easier than the axis along [110]. After implanting with 3.0×10^{16} N_2^+/cm^2 and 3.5×10^{16} N_2^+/cm^2 (not represented here) at 26 keV, the magnetization curves of the implanted samples are very similar in shape. The previously observed trend about the coercivity, the saturation field, and the reduced magnetization becomes more important with increasing fluence. The region where the magnetization changes linearly with the applied magnetic field is larger. Besides, the magnetic behavior becomes quasi-isotropic in the plane of the thin films. For 5.3×10^{16} N_2^+/cm^2 at 40 keV, the magnetic behavior of the thin film is similar to that of the implanted samples with 3.0×10^{16} N_2^+/cm^2 and 3.5×10^{16} N_2^+/cm^2 at 26 keV. It is worth noting that the magnetization curves for the implanted samples with 3.0×10^{16} N_2^+/cm^2 and 3.5×10^{16} N_2^+/cm^2 at 26 keV, and 5.3×10^{16} N_2^+/cm^2 at 40 keV are characteristic of thin films with magnetic stripe domains.[11,19] These loops display a region where the magnetization changes linearly with the applied magnetic field and low remanence. The differences in shape of the hysteresis loops reflect the disappearance of the bcc iron MCA and the appearance of a PMA generated by nitrogen implantation.[10] This PMA may come from the bct α'-Fe-N MCA, and from stress-induced anisotropy due to ion implantation.[20] Concerning out-of-plane measurements, the axis along [001] is harder than the in-plane axes due to the thin film shape anisotropy for all the conditions of ion implantation. The demagnetizing energy is therefore higher than the perpendicular density energy.

Figure 4 shows magnetic parameter values of the as-grown sample and the nitrogen-implanted samples for N_2^+ at 26 and 40 keV as a function of the fluence. As mentioned earlier, the coercivity and the saturation field are higher and the reduced magnetization at remanence is lower with increasing fluence from 1.8×10^{16} to 3.5×10^{16} N_2^+/cm^2 at 26 keV. Moreover, these parameters reach extreme values for 5.3×10^{16} N_2^+/cm^2 at 40 keV. It is interesting to observe that the coercivity and the remanence vary the most sharply for a fluence of between 1.8×10^{16} N_2^+/cm^2 and 2.2×10^{16} N_2^+/cm^2, and the saturation field varies most sharply for a fluence between 2.2×10^{16} N_2^+/cm^2 and 3.0×10^{16} N_2^+/cm^2 whatever in-plane axis is chosen. Regarding the overall loss of in-plane anisotropy, the reduced magnetization along [100] and [110] converges towards the same value for a lower fluence with N_2^+ at 26 keV in comparison to the saturation magnetization. However, the coercivity is slightly different along [100] and [110] for 3.0×10^{16} N_2^+/cm^2 and 3.5×10^{16} N_2^+/cm^2 at 26 keV.

D. Magnetic stripe domains

As shown in Fig. 5, magnetic force microscopy (MFM) measurements revealed the presence of magnetic stripe domains at remanence, as expected for the samples implanted with 3.0×10^{16} N_2^+/cm^2 and 3.5×10^{16} N_2^+/cm^2 at 26 keV, and 5.3×10^{16} N_2^+/cm^2 at 40 keV. This structure of stripe domains with alternating "up-down" magnetization is favored in PMA thin films with a thickness larger than a critical value[6] as notably shown in Fe-Ga.[11,21] The stripes are relatively straight and the period of the pattern is in the range of

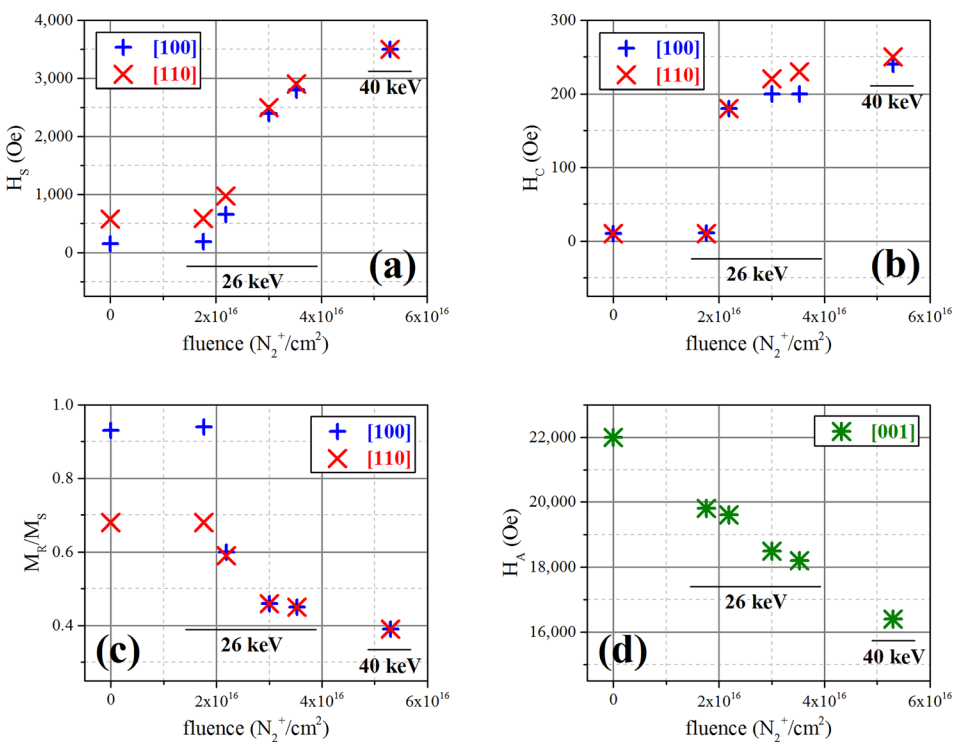

FIG. 4. Summary of the magnetic properties of Fe-N films as a function of fluences. (a) saturation field, (b) coercive field, (c) remanence ratio (M_R/M_S), and (d) anisotropy field.

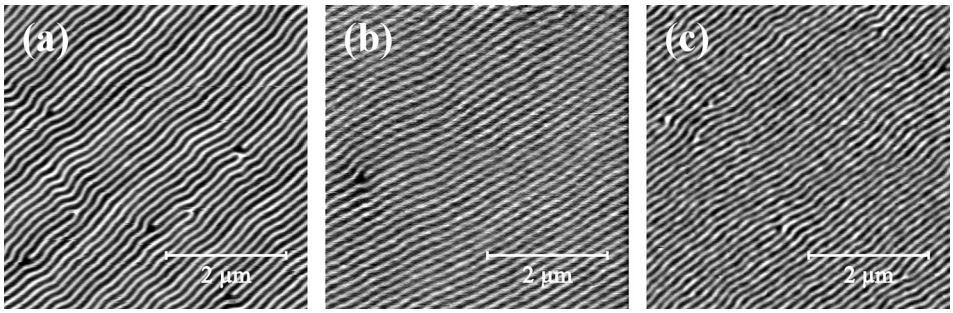

FIG. 5. Stripe pattern in Fe-N films: (a) Fe-N, 3.0×10^{16} N_2^+/cm^2 (26 keV), (b) Fe-N, 3.5×10^{16} N_2^+/cm^2 (26 keV), and (c) Fe-N, 5.3×10^{16} N_2^+/cm^2 (40 keV).

120 nm to 130 nm. Topological defects, looking like bifurcations on the MFM images, are present.

E. Magnetic anisotropy constants

The FMR measurements were performed with a commercial BRUKER ELEXSYS 500 spectrometer at X-band and Q-band frequencies. All measurements were done at room temperature. Samples of typically (1×1) mm^2 size were measured in the in-plane (rotation axis [001]) and out-of-plane (rotation axis [110]) configurations, respectively. In Fig. 6, we show the definition of the different polar (θ, θ_H) and azimuthal angles (ϕ, ϕ_H); (θ, ϕ) and (θ_H, ϕ_H) represent the orientation of the magnetization M and the applied magnetic field H, respectively, to the film normal. The two rotation planes explored in the FMR measurements are also indicated.

All samples showed one dominant uniform mode spectrum, which was used to deduce the anisotropy constants.

The FMR spectra were analyzed with the Smit Beljers formalism,[22] which allows calculating the resonance frequencies from the derivatives of the free energy density F

$$F = \frac{1}{2}M\Big[-2H[\cos\theta\cos\theta_H + \sin\theta\sin\theta_H\cos(\phi-\phi_H)] + 4\pi M\cos^2\theta - H_U^{OP}\cos^2\theta - \frac{1}{2}H_4^{OP}\cos^4\theta - \frac{1}{2}H_4^{IP}\frac{1}{4}\times(3+\cos 4\phi)\sin^4\theta - H_U^{IP}\sin^2\theta\sin^2\left(\phi-\frac{\pi}{4}\right)\Big], \quad (1)$$

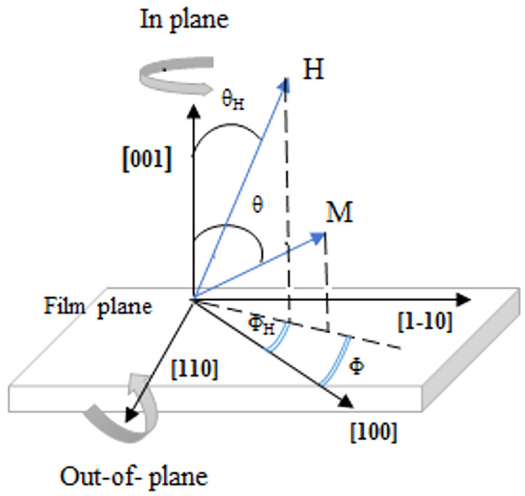

FIG. 6. Coordinate system of the in-plane and out-of-plane rotation, FMR experiments.

where H_U^{OP} and H_4^{OP} are the perpendicular uni-axial and perpendicular cubic anisotropy fields, respectively. H_U^{IP} and H_4^{IP} represent the in-plane uniaxial and in-plane cubic anisotropy fields, respectively

$$\left(\frac{\omega}{\gamma}\right)^2 = \frac{1}{M_s^2\sin^2\theta}\left[\frac{\partial^2F}{\partial\theta^2}\frac{\partial^2F}{\partial\phi^2} - \left(\frac{\partial^2F}{\partial\theta\partial\phi}\right)^2\right]. \quad (2)$$

ω is the angular frequency of the microwave field, γ is the gyromagnetic ratio, and M_s is the saturation magnetization.

The derivatives are calculated at the equilibrium positions of the magnetization (θ, ϕ).

In the case where the magnetic field and magnetization are along one of the four high symmetry axes orientation, we obtain the four Eqs. (3)–(6). (H//[001], [100], [110] and [1–10], respectively). Where H_{res} is the resonance field

$$\left(\frac{\omega}{\gamma}\right)^2 = \left(H_{res} - 4\pi M + \frac{2K_U^{OP}}{M} + \frac{2K_4^{OP}}{M}\right)\times\left(H_{res} - 4\pi M + \frac{2K_U^{OP}}{M} + \frac{2K_4^{OP}}{M} - \frac{2K_U^{IP}}{M}\right), \quad (3)$$

$$\left(\frac{\omega}{\gamma}\right)^2 = \left(H_{res} + \frac{2K_4^{IP}}{M}\right)\times\left(H_{res} + 4\pi M - \frac{2K_U^{OP}}{M} + \frac{2K_4^{IP}}{M} + \frac{K_U^{IP}}{M}\right), \quad (4)$$

$$\left(\frac{\omega}{\gamma}\right)^2 = \left(H_{res} - \frac{2K_4^{IP}}{M} - \frac{2K_U^{IP}}{M}\right)\times\left(H_{res} + 4\pi M - \frac{2K_U^{OP}}{M} + \frac{K_4^{IP}}{M}\right), \quad (5)$$

$$\left(\frac{\omega}{\gamma}\right)^2 = \left(H_{res} - \frac{2K_4^{IP}}{M} + \frac{2K_U^{IP}}{M}\right)\times\left(H_{res} + 4\pi M - \frac{2K_U^{OP}}{M} + \frac{K_4^{IP}}{M} + \frac{2K_U^{IP}}{M}\right). \quad (6)$$

From the resonance positions of the three high symmetry in-plane magnetic field orientations [100], [110], and [1–10], the three anisotropy constants K_U^{IP} (in-plane uniaxial anisotropy constant), K_U^{OP} (Out- of-plane uniaxial anisotropy constant), and K_4 have been determined. The cubic anisotropy constant K_4 has been assumed to be isotropic. The Landé g-value was set to $g = 2.09$ as for pure iron.[23]

In Fig. 7, we show typical in-plane FMR spectra for the Fe reference layer and N-implanted layers. We observe that

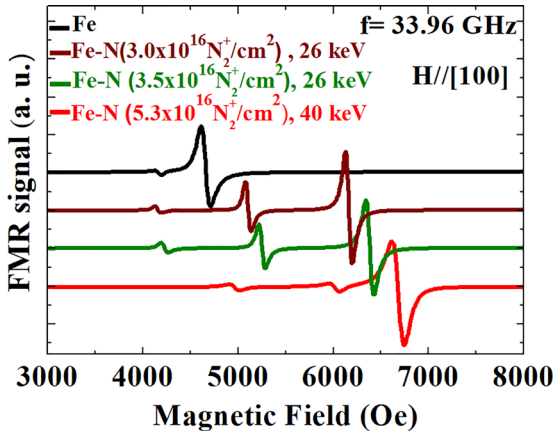

FIG. 7. Q-band FMR spectra for H//[100] for the Fe reference film (black) and three implanted bct α'-Fe-N films (red, green, and brown).

in the nitrogen-implanted iron films, the resonance fields for the in-plane orientation are shifted to higher fields as compared to the Fe film due to the modified anisotropy constants. We observe further that the in-plane anisotropy is reduced as compared to the Fe reference sample, but for all samples studied, the easy in-plane axis remains the [100] axis, which indicates that the cubic K_4 anisotropy constant remains positive.

Figure 8 represents the in-plane angular variation of the resonance field for the as-grown and nitrogen-implanted samples. These plots reveal that an in-plane magnetic anisotropy still exists for these implanted thin films even though the VSM measurements show an in-plane quasi-isotropic behavior.

In Fig. 9, we show equally some X-band out-of-plane FMR spectra, which demonstrate the decreasing resonance fields with increasing N content in agreement with the increasing uniaxial anisotropy constants deduced from the Q-band in-plane spectra (shown in Fig. 8).

In Figs. 10–12, we show the variation of the three anisotropy constants as a function of fluence. The results from samples implanted with different N_2^+ energies are distinguished by different background colors. As a matter of comparison, we report in the insets of the same figures the values obtained for MBE grown Fe-Ga epitaxial films of the

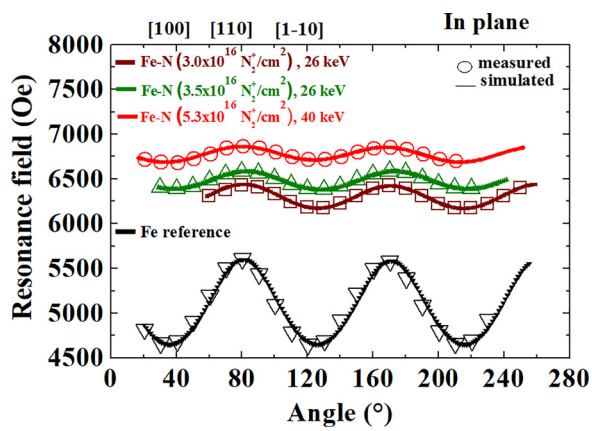

FIG. 8. Angular variation of the Q-band FMR spectra for different N contents.

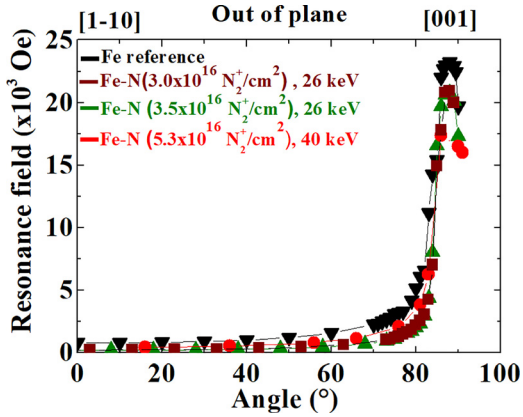

FIG. 9. Angular variation of the X-band out-of-plane FMR spectra for different N contents.

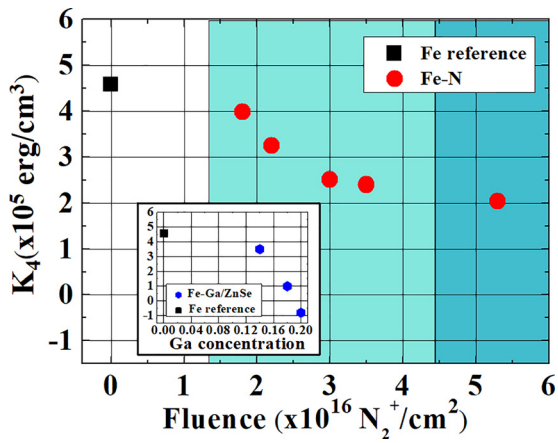

FIG. 10. Cubic anisotropy constant K_4 in N-implanted iron thin films as a function of fluence and their comparison (inset) to the case of Fe-Ga.[9]

same thickness and reported in the reference.9 The reader has to consider that Fe-Ga was obtained by MBE co-deposition of Fe and Ga and not by ion implantation.[9]

The cubic and uniaxial magnetic anisotropy constants K_4, K_U^{IP}, and K_U^{OP} are all modified by the N implantation. K_4 decreases monotonously from 4.5×10^5 erg/cm^3 to 2×10^5 erg/cm^3 and saturates for N contents higher than

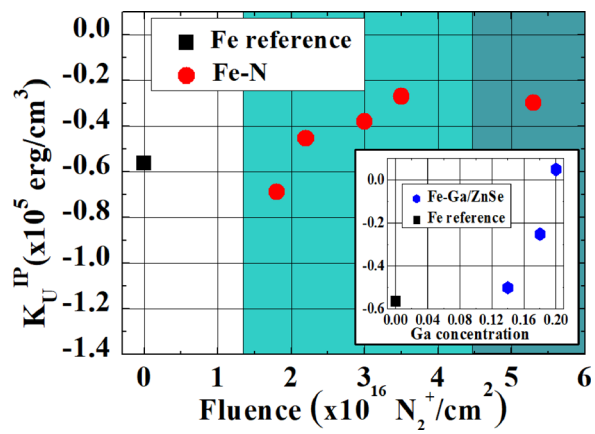

FIG. 11. In-plane uniaxial anisotropy constant K_U^{IP} in N-implanted iron thin films as a function of fluence and their comparison (inset) to the case of Fe-Ga.[9]

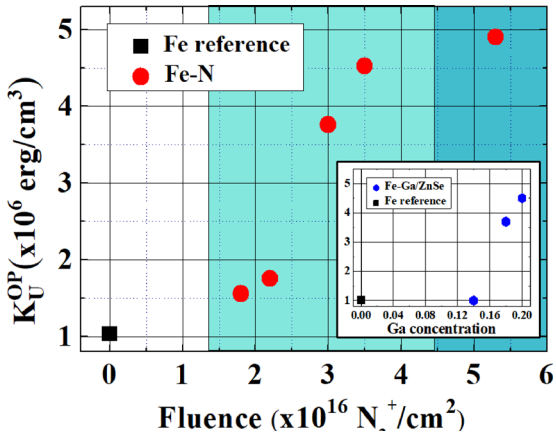

FIG. 12. Perpendicular magnetic anisotropy constant (PMA) K_U^{OP} in N-implanted iron thin films as a function of fluence and their comparison (inset) to the case of Fe-Ga.[9]

$x = 0.10$; this variation and, in particular, its saturation are different from the behavior observed in MBE grown Fe-Ga thin films of the same thickness, where K_4 continues to decrease and even switches sign at higher Ga concentrations. A possible explanation might be sought in the disordered N distribution to be expected in the N implanted films, whereas the Ga distribution in the Fe-Ga films has shown to be highly ordered. The in-plane uniaxial anisotropy constant, due to the Fe-Se bonding at the interface,[24,25] varies from -6×10^4 erg/cm^3 to values close to 0.3×10^4 erg/cm^3 which renders the [110] and [1–10] orientations equivalent. The most important variation is observed for the uniaxial out-of-plane anisotropy constant, which increases from 1.0×10^6 erg/cm^3 to 4.9×10^6 erg/cm^3. The weak out of plane uniaxial anisotropy present in the non-implanted film is due to the ZnSe/Fe interface bonding. From 1.8×10^{16} to 3.5×10^{16} N_2^+/cm^2 at 26 keV, K_U^{OP} increases with increasing fluence. This phenomenon is notably related to the formation of bct α'-Fe-N whose c-axis is perpendicular to the thin film plane and the c-parameter increases with fluence. Moreover, K_U^{OP} rises sharply when the c-parameter of α'-Fe-N becomes close to that of α'-Fe$_8$N. For 5.3×10^{16} N_2^+/cm^2 at 40 keV, K_U^{OP} reaches its maximum value. Nitrogen penetrates deeper into the thin film when the ion energy is higher. Hence, this increase of K_U^{OP} may be due to differences in amount and distribution of α'-Fe-N in the thin films.

IV. CONCLUSION

In conclusion, the magnetic properties of nitrogen-implanted iron thin films grown by MBE on ZnSe/GaAs (001) have been investigated for different sets of implantation parameters. We have shown that nitrogen implantation induces changes in the magnetic anisotropies of iron thin films depending on ion energy and fluence. These magnetic changes are related to the structural modifications induced by ion implantation. A PMA appeared in implanted samples and may originate from the MCA of nitrogen-martensite whose c-axis is perpendicular to the thin films plane and/or stress anisotropy. For N_2^+ at 26 keV, the PMA and the c-parameter of nitrogen-martensite increase with fluence. It is worth noting that this PMA rises strongly when the c-parameter of nitrogen-martensite is close to that of α'-Fe$_8$N. For N_2^+ at 40 keV, a maximum value of the PMA of 4.9×10^6 erg/cm^3 is found. In comparison with the highest fluence at 26 keV, this PMA increase may be due to differences in amount and depth distribution of nitrogen-martensite in the thin films. Interestingly, the PMA in Fe-N thin films is of the same order of magnitude as in Fe-Ga thin films. Furthermore, magnetic stripe domains, like those in Fe-Ga samples, have been observed in Fe-N samples presenting differences in PMA. As a consequence of this work, nitrogen-martensite thin films presenting both tunable PMA and magnetic stripe domains can be made by ion implantation in order to develop modern magnetism applications.

ACKNOWLEDGMENTS

The authors would like to thank Dr. Frans Munnik and Dr. René Heller of Helmholtz-Zentrum Dresden-Rossendorf for ERDA and RBS measurements. The authors also acknowledge Paola Atkinson for preparing the GaAs substrate by MBE, Dominique Ledu for doing the implantation, Sarah Hidki for carrying out the XRD measurements, and Ian Vickridge for helpful discussion. This work was partially supported by the SPINSAW Project (No. ANR 13-JS04–0001-01) and the MATINNOV industrial chair (No. ANR-12-CHIN-0004) of the French National Research Agency (ANR). T. Amarouche expresses her gratitude to Neo-Tech SA for their support.

[1]S. Mangin, D. Ravelosona, J. A. Katine, M. J. Carey, B. D. Terris, and E. E. Fullerton, Nat. Mater. **5**, 210 (2006).
[2]H. Meng and J. P. Wang, Appl. Phys. Lett. **88**, 172506 (2006).
[3]S. Yakata, H. Kubota, Y. Suzuki, K. Yakushiji, A. Fukushima, S. Yuasa, and K. Ando, J. Appl. Phys. **105**, 07D131 (2009).
[4]L. J. Zhu, S. H. Nie, K. K. Meng, D. Pan, J. H. Zhao, and H. Z. Zheng, Adv. Mater. **24**, 4547 (2012).
[5]L. J. Zhu and J. H. Zhao, Appl. Phys. A **111**, 379 (2013).
[6]A. Hubert and R. Schäfer, *Magnetic Domains: The Analysis of Magnetic Microstructures* (Springer, Berlin, 1998).
[7]U. Ebels, L. D. Buda, K. Ounadjela, and P. E. Wigen, "Small amplitude dynamics of nonhomogeneous magnetization distributions: the excitation spectrum of stripe domains," in *Spin Dynamics in Confined Magnetic Structures I*, edited by B. Hillebrands and K. Ounadjela (Springer-Verlag, Berlin, 2002), pp. 167–217.
[8]N. Ji, M. S. Osofsky, V. Lauter, L. F. Allard, X. Li, K. L. Jensen, H. Ambaye, E. Lara-Curzio, and J.-P. Wang, Phys. Rev. B **84**, 245310 (2011).
[9]M. Barturen, J. Milano, M. Vásquez-Mansilla, C. Helman, M. A. Barral, A. M. Llois, M. Eddrief, and M. Marangolo, Phys. Rev. B **92**, 054418 (2015).
[10]L.-C. Garnier, M. Eddrief, S. Fin, D. Bisero, F. Fortuna, V. H. Etgens, and M. Marangolo, SPIN **6**, 1640014 (2016).
[11]M. Barturen, B. Rache Salles, P. Schio, J. Milano, A. Butera, S. Bustingorry, C. Ramos, A. J. A. de Oliveira, M. Eddrief, E. Lacaze, F. Gendron, V. H. Etgens, and M. Marangolo, Appl. Phys. Lett. **101**, 092404 (2012).
[12]K. Nakajima and S. Okamoto, Appl. Phys. Lett. **56**, 92 (1990).
[13]K. H. Jack, Proc. R. Soc. London, Ser. A **208**, 200 (1951).
[14]H. Takahashi, M. Igarashi, A. Kaneko, H. Miyajima, and Y. Sugita, IEEE Trans. Magn. **35**, 2982 (1999).
[15]M. Takahashi and H. Shoji, J. Magn. Magn. Mater. **208**, 145 (2000).
[16]M. Eddrief, Y. Zheng, S. Hidki, B. Rache Salles, J. Milano, V. H. Etgens, and M. Marangolo, Phys. Rev. B **84**, 161410(R) (2011).
[17]N. P. Barradas, C. Jeynes, and R. P. Webb, Appl. Phys. Lett. **71**, 291 (1997).

[18]J. F. Ziegler, J. P. Biersac, and U. Littmark, *The Stopping and Range of Ions in Solids* (Pergamon, New York, 1985).
[19]N. Saito, H. Fujiwara, and Y. Sugita, J. Phys. Soc. Jpn. **19**, 1116 (1964).
[20]K. Nakajima and S. Okamoto, Appl. Phys. Lett. **54**, 2536 (1989).
[21]S. Fin, R. Tomasello, D. Bisero, M. Marangolo, M. Sacchi, H. Popescu, M. Eddrief, C. Hepburn, G. Finocchio, M. Carpentieri, A. Rettori, M. G. Pini, and S. Tacchi, Phys. Rev. B **92**, 224411 (2015).
[22]J. Smith and H. G. Beljers, Philips Res. Rep. **10**, 113 (1955).
[23]Kh. Zakeri, Th. Kebe, J. Lindner, and M. Farle, J. Magn. Magn. Mater. **299**, L1 (2006).
[24]M. Marangolo, F. Gustavsson, G. M. Guichar *et al*., Phys. Rev. B **70**, 134404 (2004).
[25]E. Sjostedt, L. Nordstrom, F. Gustavsson, and O. Eriksson, Phys. Rev. Lett. **89**, 267203 (2002).